CrystEngComm

ROYAL SOCIETY OF CHEMISTRY

PAPER

View Article Online
View Journal | View Issue

Cite this: *CrystEngComm*, 2024, **26**, 349

Self-organized formation of seven-rod bundle morphology for lanthanum Prussian blue analog microcrystals *via* a precipitation process†

Fumiyuki Shiba, * Ren Nagata and Yusuke Okawa

Received 14th November 2023,
Accepted 10th December 2023

DOI: 10.1039/d3ce01140b

rsc.li/crystengcomm

This article reports potassium lanthanum hexacyanidoferrate(II) microcrystals with a unique shape consisting of seven hexagonal rods. In an aqueous solution at 55 °C, $[Fe(CN)_6]^{3-}$ ions were reduced by ascorbic acid to form $[Fe(CN)_6]^{4-}$ ions, which reacted with the surrounding K^+ and La^{3+} ions to generate $K_{0.82}La_{1.11}[Fe(CN)_6]\cdot 4H_2O$ microcrystals. The morphology was spontaneously constructed without growth modifiers *via* the instantaneous precipitation of the Prussian blue analog with a hexagonal crystal structure under a specific range of reaction conditions.

Introduction

The morphology of crystalline substances, for both natural minerals and synthesized materials, has attracted our interest for a long time. Single crystalline solids have been the center of interest because they tend to show polygonal crystal habits reflecting the crystal structures. For example, on microcrystals synthesized in the aqueous phase, substances with a cubic crystal lattice, such as AgCl,[1] are likely to have a cubic shape. Prussian blue, $Fe_4[Fe(CN)_6]_3\cdot nH_2O$, and some of its analogs (PBAs) also tend to be cubic, reflecting their cubic crystal structures.[2] Hexagonal prism shapes are often observed for the hexagonal structure materials such as rhabdophane-type YPO_4 microcrystals.[3,4]

The crystal habit of microcrystals is usually determined thermodynamically or kinetically based on the crystal structure as a fundamental factor.[5,6] In the former cases, called equilibrium forms, the lattice planes with low specific surface energies preferentially appear as the facets of the polyhedral crystal to minimize its overall surface energy, as formulated by Wulff's theorem. In the latter cases, called growth forms, on the other hand, the difference in the growth rate among the surfaces determines the morphology; slow growth rate surfaces remain as the facets by vanishing faster growing ones to become the edges or the corners. The growth forms would be more significant on morphology control since the growth rate constants are expected to be changed more efficiently by changing the reaction conditions, using growth modifiers, or introducing screw dislocations or twins.

Reaction conditions usually determine the growth rates of crystal planes. On AgBr microcrystals (NaCl-type structure), for example, the growth rates for the {100} and {111} faces depend on pBr (≡ $-\log[Br^-]$) but have different dependence on pBr.[7] Although the growth rates for both faces show a minimum around pBr 3.3 corresponding to the solubility minimum, the growth rate ratio of the {100} face to the {111} face is monotonously increased with a decrease of pBr (*i.e.*, increase of free Br^- ion concentration); the ratio is almost unity around pBr 3. As a result, the morphology of AgBr changes from cubic at around pBr 4 to octahedral at around pBr 2. At the intermediate region of around pBr 3, cuboctahedral microcrystals are formed.

The morphology can also be attributed to the reaction temperature. For example, a temperature-dependent height/width ratio has been reported for rhabdophane-type YPO_4 microcrystals with a hexagonal prism shape synthesized in a hydrothermal system with sodium citrate.[4] The activation energies for width- and height-direction growths are estimated as 97 kJ mol^{-1} and 112 kJ mol^{-1}, corresponding to the larger width/height ratio at a lower reaction temperature.

Using growth modifiers, whether constituent ions or additives, often enables us to control the morphology more effectively. Hamada *et al.* reported the synthesis of monodisperse star-like Cu_2O microcrystals that consist of six square pyramids orthogonally aligned with each other in an aqueous system containing 1,2-ethylenediamine and hexamethylenetetramine.[8] Chen *et al.* hydrothermally synthesized Cu_2O microcrystals under various reaction conditions, including the kind of additives, to form a variety of morphologies, including regular and truncated polyhedra, hopper crystals, multi-pod branching structures, *etc.*[9] Sodium

Department of Materials Science, Chiba University, 1-33 Yayoicho, Inageku, Chiba 263-8522, Japan. E-mail: shiba@faculty.chiba-u.jp

† Electronic supplementary information (ESI) available: Details for the composition evaluations and outer plane angle estimations. See DOI: https://doi.org/10.1039/d3ce01140b

acetate contributes to making the width narrower for wedge-like α-GaOOH microcrystals synthesized *via* the hydrolysis process.[10] Maskasky prepared seven different kinds of polyhedra for AgBr microcrystals with a cubic crystal lattice by using appropriate organic substances that specifically inhibit the growth of the respective surface.[11]

In this article, we describe the self-organized formation of uniquely shaped microcrystals of potassium lanthanum hexacyanidoferrate(II) (KLa-HCF), a kind of PBA.

Experimental

Materials

All chemicals used in the present study were purchased from FUJIFILM Wako Pure Chemical Co., Japan, except for xylenol orange (XO) from Dojindo Laboratories, Japan. The chemicals were used without additional purifications.

Synthesis of KLa-HCF microcrystals

In a glass reaction vessel, 0.04 mol L^{-1} $K_3[Fe(CN)_6]$ aqueous solution (5 mL) was mixed with 0.02 mol L^{-1} $La(NO_3)_3$ aqueous solution (10 mL) under magnetic stirring at 55 °C kept in a water bath. Then, 0.2 mol L^{-1} ascorbic acid (AscA) aqueous solution (5 mL) was introduced into it using a micropipette (time for addition *ca.* 1 s). Thus, the reactant concentrations after mixing for $La(NO_3)_3$, $K_3[Fe(CN)_6]$, and AscA were C_{La} = 0.01 mol L^{-1}, C_{HCF} = 0.01 mol L^{-1}, and C_{AscA} = 0.05 mol L^{-1}, respectively. After 30 min, the precipitate was separated from the aqueous phase by suction filtration, and the precipitate was freeze-dried.

Characterization of the microcrystal morphology and structure

The microcrystals were observed with an FE-SEM (JEOL JSM-6700F) operated at 15 kV. To prepare the specimen for the FE-SEM observation, the freeze-dried powder of the microcrystals was put on electrically conductive double-sided carbon tape on a brass specimen stub. The specimen was coated with Pt by sputtering before observation. To evaluate the crystal structure of the microcrystals, the freeze-dried powder was subjected to powder XRD measurement using a Bruker D8 Advance with Cu Kα radiation (λ = 1.5418 Å: 40 kV × 40 mA = 1600 W). Selected area electron diffraction (SAED) patterns were obtained with a TEM (Hitachi H-7650) operated at 100 kV.

Evaluation for the elemental composition of the microcrystals

The elemental composition of the microcrystal was evaluated by atomic absorption spectrometry (AAS) for K^+ and Fe (of $[Fe(CN)_6]^{4-}$) and by colorimetry for La^{3+}. The accurately weighed KLa-HCF powder (25 mg) was dissolved in 2.5 mL of 1 mol L^{-1} HNO_3 and then diluted with distilled water to appropriate concentrations of analyses. The AAS determination was conducted using a Varian SpectrAA 55 with the acetylene/air flame. The absorption lines employed were λ = 404.4 nm and 248.3 nm for K and Fe, respectively. On the colorimetry for La^{3+}, xylenol orange (XO) was used as the coloring agent in the presence of cetylpyridinium chloride (CPC) at pH 8.65 (ref. 12) (see the ESI† for details).

The number of hydrated water molecules in the KLa-HCF lattice space was estimated by TG–DTA analysis with a Seiko Instruments TG/DTA6300 at 10 °C min^{-1} (the DTA reference: Al_2O_3).

Results and discussion

Fig. 1 shows FE-SEM images for the KLa-HCF microcrystals in the present procedure. Many of the formed microcrystals are in a morphology that resembles a rod bundle shape, as shown in the broad range view in Fig. 1(a). The close-up view, Fig. 1(b)–(d), indicates that each microcrystal is constructed with seven rods; the surrounding six outer rods are connected to the center rod. Each outer rod consists of two stems growing from a bulge at the midpoint of the rod, as shown in Fig. 1(c). The stems become wider toward the rod tips. The top-down view image, Fig. 1(d), indicates that the cross-section of each stem is hexagonal, and the diagonal lines of the hexagons are aligned in the same direction among the seven rods.

The XRD pattern for the present microcrystals, Fig. 2, is matched with that for $KLa[Fe(CN)_6]\cdot 4H_2O$ (ICDD PDF 00-038-0710; hexagonal lattice; space group $P6_3/m$). The lattice parameters are estimated as a = 7.41 Å and c = 14.06 Å from the d-spacings for the 102 and 110 reflections in Fig. 2. The lattice parameter values are in good agreement with those in the literature (a = 7.408 Å and c = 13.934 Å in the PDF data; a = 7.3829 Å and c = 13.871 Å in ref. 13). The hexagonal crystal structure accords with the hexagonal shape of the rod's cross-sections shown in Fig. 1(d), suggesting that the lateral and height directions of the rod correspond to the a- and c-axis directions of the hexagonal lattice, respectively.

The orientation is also confirmed by the SAED patterns shown in Fig. 3; the insets are the microcrystals subjected to the SAED measurements. In Fig. 3(a), Laue spots align in a rectangle arrangement; the distances between the adjacent spots along the height direction correspond to d =14.2 Å of the lattice spacing, which is almost the same as the lattice parameter of c (= 14.06 Å) estimated from the XRD pattern. In Fig. 3(b), on the other hand, the Laue spots suggest a 6-fold symmetry of the crystal structure in the cross-sectional hexagonal planes. Also, from the estimated lattice spacings, the $\{1\bar{2}10\}$ planes stack towards the hexagon's corner directions. Thus, the morphological feature concurs with the ion arrangement in the microcrystals, although the splitting Laue spots by double diffraction in Fig. 3(a) and (b) imply that the microcrystals may have some imperfections.

Even with the unique morphology, the facets would be related to the lattice planes of the crystal. Although the angle of the side face of the rod to the c-axis is different at the position along the height direction, it is about 23°, close to 28° for the $\{10\bar{1}1\}$ planes, around the concaves that divide

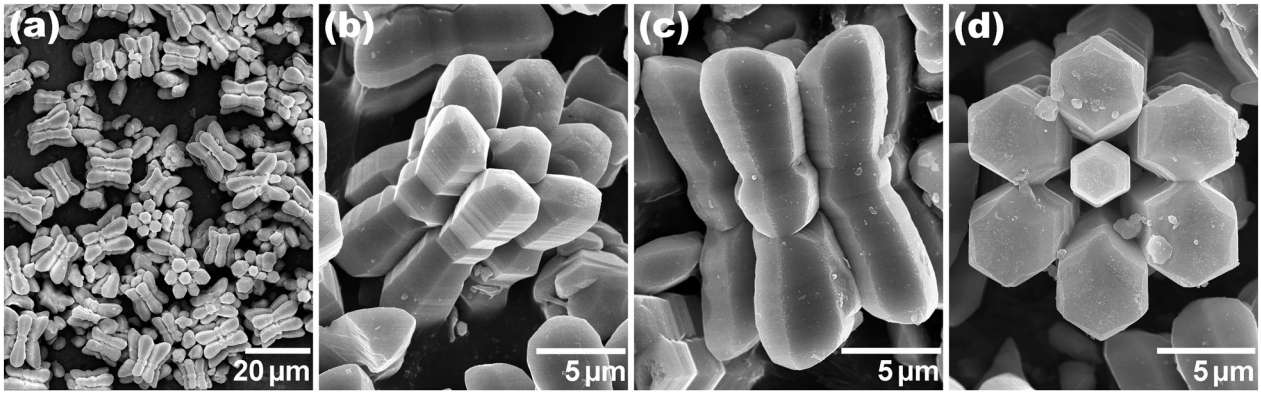

Fig. 1 FE-SEM images of the potassium lanthanum hexacyanidoferrate microcrystals precipitated from the mixed solution of $La(NO_3)_3$ and $K_3[Fe(CN)_6]$ *via* the reduction reaction by ascorbic acid. (a) A broad range view and close-up views from (b) tilted, (c) side, and (d) top-down angles.

the rod into the bulge and the stems (Fig. S1 in the ESI†). It is reasonable that the facet is the $\{10\bar{1}1\}$ plane, as the 101 reflection is observed in the XRD pattern in Fig. 2. The angle decrease around the stem tips could be due to the appearance of other indexed faces. In addition, the fringes on the stems shown in Fig. 1(b) would suggest the formation of lamellar twins on the {0001} faces, also contributing to the decrease of the angle.

Since PBAs possibly have compositions deviating from the stoichiometric formulae,[14] the elemental composition of the present microcrystals was evaluated by dissolving the freeze-dried powder in HNO_3 to apply the AAS (K^+ and $[Fe(CN)_6]^{4-}$) and colorimetry (La^{3+}) measurements. The estimated composition formula is $K_{0.82}La_{1.11}[Fe(CN)_6]$, which seems to be in the reasonable range of experimental estimation for the ions, as the total cation valence (+4.17) is close to the anion valence (−4).

The number of hydrated water molecules, n, was determined by TG-DTA measurement as shown in Fig. 4. According to the literature, the endothermic weight decrease up to 260 °C is associated with the dehydration of the hydrated water; the decrease above 300 °C is related to the decomposition of CN.[13,15] For $K_{0.82}La_{1.11}[Fe(CN)_6]$, n = 3.96 is obtained from the weight loss in the former process, 15.2%. The n value agrees with the literature, n = 4. Therefore, the compositional formula of the present microcrystals may be denoted as $K_{0.82}La_{1.11}[Fe(CN)_6]\cdot 4H_2O$.

Interestingly, this unique morphology of KLa-HCF microcrystals was spontaneously formed under a simple precipitation process described in the experimental section. The microcrystal precipitation was triggered by the AscA addition into the mixed solution of $La(NO_3)_3$ and $K_3[Fe(CN)_6]$: La^{3+} ions were unreactive with $[Fe(CN)_6]^{3-}$ ions, at least under the present conditions; thus the mixed solution was stable until AscA was added. Introducing the AscA solution, the transparent yellowish color of $[Fe^{III}(CN)_6]^{3-}$ ions vanished immediately by reduction to $[Fe^{II}(CN)_6]^{4-}$ ions as:

$$2[Fe^{III}(CN)_6]^{3-} + C_6H_8O_6 \rightarrow 2[Fe^{II}(CN)_6]^{4-} + C_6H_6O_6 + 2H^+, \quad (1)$$

where $C_6H_8O_6$ and $C_6H_6O_6$ are ascorbic acid and dehydroascorbic acid, respectively. The $[Fe^{II}(CN)_6]^{4-}$ ions reacted with the surrounding La^{3+} ions to form KLa-HCF microcrystals, making the reacting solution turbid.

The turbidity continued to increase for about 10 s, suggesting that the crystallization process was completed at least within a few minutes. In fact, the microcrystals sampled at 1 min seem to be the same as those at 30 min in their

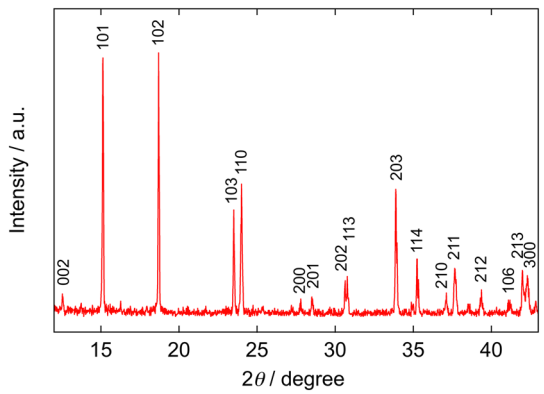

Fig. 2 XRD pattern for the KLa-HCF microcrystals shown in Fig. 1 (Cu Kα radiation; λ = 1.5418 Å). The peaks are matched with the reference data for $KLa[Fe(CN)_6]\cdot 4H_2O$ (ICDD PDF 00-038-0710).

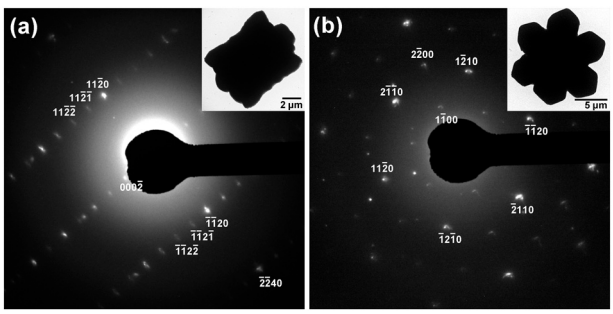

Fig. 3 Selected area electron diffraction patterns for the single KLa-HCF microcrystals indicated in the insets. The patterns correspond to those for the (a) [1$\bar{1}$0] and (b) [00$\bar{1}$] incident directions of the electron beam.

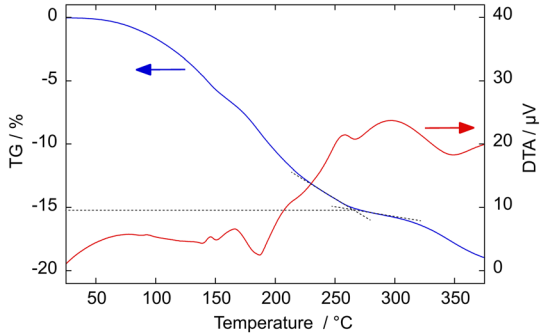

Fig. 4 TG–DTA result for the KLa-HCF microcrystals with a seven-rod bundle morphology. The 15.2% weight loss up to 260 °C is due to the dehydration process of the hydrated water.

morphology and size, as shown by the FE-SEM images in Fig. S2 in the ESI.† Owing to the H^+ ion generation by the reduction process, the pH after the reaction (pH 2.04; after 30 min from the AscA addition) was lower than that even for the AscA solution (pH 2.36).

Although the present procedure using $K_3[Fe(CN)_6]$ with AscA has practical advantages for effectively forming the seven-rod bundle morphology of the microcrystals, the low pH seems significant in generating them, rather than the reduction reaction by AscA. Using $K_4[Fe(CN)_6]$ instead of $K_3[Fe(CN)_6]$ enables us to precipitate KLa-HCF microcrystals without using AscA, as shown in Fig. 5 (C_{La} = C_{HCF} = 0.01 mol L^{-1}, 55 °C). Removing the ascorbic acid resulted in the higher reaction pH at pH 6.47, and microcrystals with a pteridophyte leaf-like shape were generated (Fig. 5(a)). Reacting at pH 2.19 by preliminarily adding HNO_3 in the $La(NO_3)_3$ solution, on the other hand, the precipitate contained rod-bundle-shaped microcrystals (Fig. 5(b)). However, their percentage was smaller than the present $K_3[Fe(CN)_6]$ system. Thus, it is suggested that the unique morphology of the present KLa-HCF microcrystals originates from their intrinsic nature of dendritic growth without the assistance of specific growth modifiers.

To evaluate the effect of reaction temperature on the morphology, the KLa-HCF microcrystals have been prepared at different temperatures using $K_3[Fe(CN)_6]$ and AscA under the conditions at C_{La} = C_{HCF} = 0.01 mol L^{-1} and C_{AscA} = 0.05

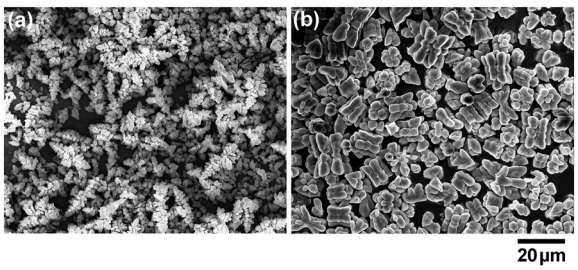

Fig. 5 FE-SEM images of KLa-HCF microcrystals prepared with $La(NO_3)_3$ and $K_4[Fe(CN)_6]$ aqueous solutions at (a) pH 6.47 without adding acid for pH adjusting and (b) pH 2.19 by adding HNO_3 to $La(NO_3)_3$ aqueous solution before mixing (reaction temperature 55 °C).

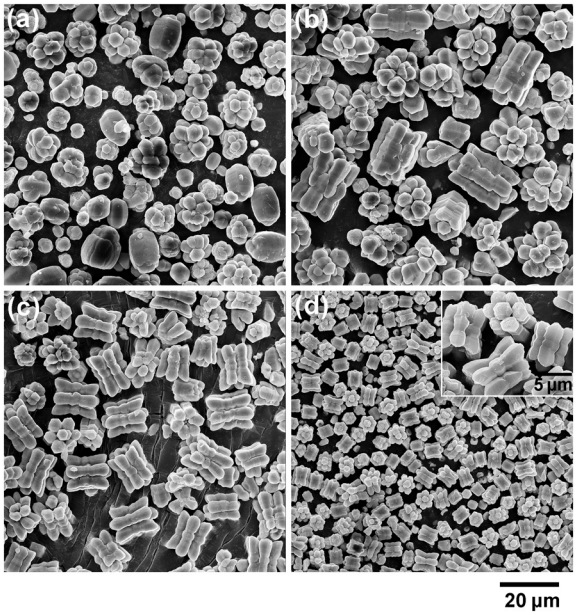

Fig. 6 FE-SEM images of the KLa-HCF microcrystals prepared at different temperatures (C_{La} = C_{HCF} = 0.01 mol L^{-1}, C_{AscA} = 0.05 mol L^{-1}). (a) 25 °C, (b) 40 °C, (c) 55 °C (control), and (d) 70 °C. The inset in (d) is the close-up view.

mol L^{-1} (reaction time 30 min). The FE-SEM images are shown in Fig. 6, where the pH values were almost the same among the temperatures: pH 2.06, 2.09, 2.09, and 2.16 at 25, 40, 55, and 70 °C, respectively. At 25 °C, Fig. 6(a), the bundle-morphology microcrystals are not observed; many nubby microcrystals are found instead. Increasing the reaction temperature increases the percentage of the bundle morphology. At 70 °C, almost all the microcrystals are in the bundle morphology, with a smaller size.

When AscA was introduced, the turbidity increased more slowly at the lower temperatures, while the yellow color of $[Fe(CN)_6]^{3-}$ vanished instantaneously even at 25 °C. This means that the temperature mainly affects the precipitation process rather than the reduction process. As the microcrystal size is determined by the number of microcrystals formed based on the mass-balance relationship, the small size at higher temperatures implies that the nucleation rate increases more significantly than the growth rate with temperature. In other words, at a lower temperature, a smaller number of microcrystals grow relatively slowly, resulting in a decreased consumption rate of the reactant. The highly supersaturated conditions maintained for a relatively long time could cause stacking faults to generate the nubby microcrystals. Hence, the conditions of the fast reaction seem to be preferred for forming the bundle morphology.

Fig. 7 shows the KLa-HCF microcrystals prepared at lower $La(NO_3)_3$ and $K_3[Fe(CN)_6]$ concentrations at C_{AscA} = 0.05 mol L^{-1} (55 °C, 30 min). The size decrease, corresponding to the decreased reactant amount, suggests that the number of microcrystals is similar among the reactant concentrations. At

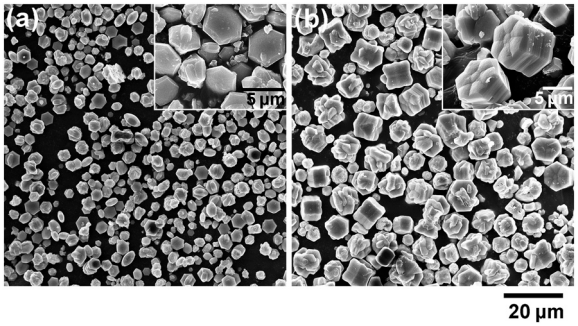

Fig. 7 FE-SEM images of KLa-HCF microcrystals prepared at 55 °C at lower reactant concentrations of $C_{La} = C_{HCF}$ = (a) 0.003 mol L^{-1} and (b) 0.001 mol L^{-1}. C_{AscA} = 0.05 mol L^{-1}. The insets are the close-up views.

$C_{La} = C_{HCF}$ = 0.001 mol L^{-1} (1/10 of the control condition), the precipitate mainly consists of hexagonal disk microcrystals with relatively thin thickness (pH 2.51). Some bundle-morphology microcrystals are found at $C_{La} = C_{HCF}$ = 0.003 mol L^{-1}, but with lower height and not-separated rods (pH 2.47). Here, the somewhat higher pH values are due to the decrease of H^+ ions generated from AscA by the reduction process.

Compared to the control condition, the turbidity increases are also slower, requiring a longer time to reach the turbidity maxima under these conditions. As the formation of $[Fe(CN)_6]^{4-}$ by AscA reduction is instantaneous, the lower reactant concentration would give a lower supersaturation condition for the KLa-HCF formation. This results in a slower reaction rate, which might be unpreferred to form the bundle morphology but preferred to avoid stacking faults. These results may lead to the tendency for the bundle morphology to be preferably formed at a fast growth rate with a high supersaturation level.

Unfortunately, the formation mechanism for the seven-rod bundle morphology is not yet clear. However, the FE-SEM images in Fig. 1 may give speculations on the self-organized formation of the microcrystals. The bulges of the six outer rods are bound to the center rod at the corner positions of the cross-sectional hexagons, as shown in Fig. 1(b)–(d). The consistently directed hexagons mean the same crystal orientation among the rods. Such morphological features seem similar to snow crystals of a sector-plane type formed under high supersaturation conditions at specific temperature regions, apart from the planar structure of the snow crystals.[16,17]

Inferring from the analogy of the snowflakes, the rod-bundle structure formation could be associated with the Berg effect, which gives a faster growth rate at the corner than the edges of a hexagonal plate by the supersaturation difference.[5,18,19] Compared to the edges, the corners protrude to the diffusion layer of a higher supersaturation region so that the growth around the corners could be selectively promoted to form new hexagons *via* dendritic growth, becoming the bulges of the outer rods. The following vertical growth from the outer bulges and the center hexagon constructs the rod bundles. The Berg effect possibly contributed also to the rod's shape; faster growth at the outer parts of the rods in a higher supersaturation resulted in the broader width with the shifted centers of cross-sectional hexagons and their tilted-up tips.

The crystal structure of KLa-HCF would be another factor for the dendritic growth that causes the seven-rod bundle morphology. The arrangement of La^{3+} and $[Fe(CN)_6]^{4-}$ ions in the $KLa[Fe(CN)_6]\cdot 4H_2O$ crystals is illustrated in Fig. 8, where the coordination data are from the literature;[13] K^+ ions and H_2O molecules, located in the interstitial space, are omitted in Fig. 8 for simplification. Note that each illustration is an overlapped view of some parallel lattice planes having different ion positions. Reflecting the large ionic radius of La^{3+}, $KLa[Fe(CN)_6]\cdot 4H_2O$ exhibits the inverse NiAs arrangement of the constituent ions (hexagonal, $P6_3/m$), in which $[Fe(CN)_6]^{4-}$ ions fill all the octahedral holes of the hcp configuration of La^{3+} ions (on the present microcrystals, some $[Fe(CN)_6]^{4-}$ positions would be vacant due to the estimated composition, $K_{0.82}La_{1.11}[Fe(CN)_6]\cdot 4H_2O$).

The ion arrangements are very different in the lattice directions. The view from the [001] direction, Fig. 8(a), indicates the hexagonal arrangement of ions; the illustrated $[Fe(CN)_6]^{4-}$ ions are located on the same lattice plane, whereas the La^{3+} ions are on two different La^{3+} planes, as indicated in Fig. 8(b). The views from the [010] and $[\bar{2}\bar{1}1]$ directions (Fig. 8(b) and (c), respectively) correspond to the observations from the corner and the edge directions of the cross-sectional hexagon, respectively. In Fig. 8(b), $[Fe(CN)_6]^{4-}$ ions are in a rectangular arrangement, but La^{3+} ions are in a parallelogram one; La^{3+} and $[Fe(CN)_6]^{4-}$ ions are located on the same plane with a relatively narrow lattice spacing, as shown in Fig. 8(c). In Fig. 8(c), both La^{3+} and $[Fe(CN)_6]^{4-}$ ions are in rectangular arrangements; La^{3+} ions and $[Fe(CN)_6]^{4-}$ ions are on different planes, as shown in Fig. 8(b).

Moreover, the C–N–La bonds are bent in the KLa-HCF lattice, as illustrated in Fig. 8. According to the coordination data obtained by single crystal X-ray diffraction, the six CN^- ions rectangularly coordinate to the center Fe^{2+} ion even in the hexagonal inverse NiAs structure of $KLa[Fe(CN)_6]\cdot 4H_2O$.[13,20] As a result, the CN^- ligands are not directed to the center of La^{3+} ions, different from the linear C–N–Fe configuration for Prussian blue, $Fe_4[Fe(CN)_6]_3\cdot nH_2O$ (cubic lattice, $Fm3m$ or $Pm3m$).[21] The structural features of KLa-HCF would cause irregular ion deposition and contribute to its dendric growth tendency and, thus, to the self-organized formation of its seven-rod bundle morphology.

KLa-HCF is a kind of PBA; PBAs are a group of substances in which other metal ions substitute either (or both) Fe ions for Prussian blue, $K_{3x}Fe^{III}_{(4-x)}[Fe^{II}(CN)_6]_3\cdot nH_2O$ (x = 0–1, typically x = 0). Though the present study has focused on the morphological interest of the lanthanum PBA, syntheses and applications of various PBAs have been widely studied owing to their functionality.[22] The substituting metal ions studied are mainly d-block transition elements such as Co, Ni, Cr, or Mn; these PBAs have been of interest in magnetic, display, and battery materials, *etc.*

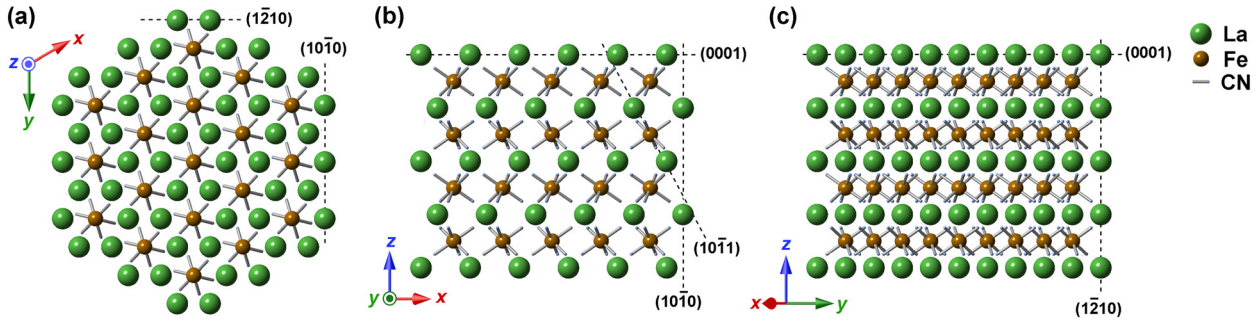

Fig. 8 The hexagonal crystal structure for $KLa[Fe(CN)_6]\cdot 4H_2O$ viewed from the (a) [001] (top), (b) [010] (corner), and (c) [$\bar{2}$10] (edge) directions, where K^+ ions and hydrated H_2O molecules located in the interstitial space are omitted for simplification. The dotted lines indicate the orientations for the indexed lattice planes vertical to the illustration. Note that the ionic radius ratio of La^{3+} to Fe^{2+} is not illustrated quantitatively. The coordination data for the atoms are based on the literature.[13]

Lanthanoid substituting PBAs, Ln-HCF, including La-HCF, are expected as precursors of $LnFeO_3$ perovskites, which can be converted from Ln-HCF by calcining at about 600 °C or higher depending on the kind of Ln.[15,23] For example, perovskite-type $LaFeO_3$ is expected to be applied to electrode materials for CO_2 reduction in solid oxide electrolysis cells,[24] catalysts for the oxygen evolution reaction,[25] *etc.* The $SmFeO_3$ perovskite has been applied to gas sensors.[26] On the other hand, on Ln-HCFs themselves, relatively small numbers of studies on microcrystal syntheses or applications seem to be reported despite the functionalities of lanthanoids.[27–29] The present study expects to trigger studies on lanthanoid Prussian blue analogs.

Conclusions

Potassium lanthanum hexacyanidoferrate(II) microcrystals formed the seven-rod bundle morphology *via* the precipitation process under acidic conditions around pH 2 without a specific growth modifier. The constituent ion arrangement on the crystal lattice framework possibly originated from the self-organized formation of the morphology with the assistance of the growth kinetics.

Author contributions

F. S. designed the study and prepared the manuscript. F. S. and R. N. synthesized and characterized the microcrystals. All the authors discussed the results.

Conflicts of interest

There are no conflicts to declare.

Acknowledgements

The authors thank Z. Li and Y. Nishinaka, Department of Materials Science, Chiba University, for the TG-DTA measurement. The XRD patterns were obtained at the Center for Analytical Instrumentation, Chiba University. This work was supported by JSPS KAKENHI Grant Number JP22K04946.

Notes and references

1 I. H. Leubner, *J. Imaging Sci.*, 1985, **29**, 219; T. Sugimoto, *Adv. Colloid Interface Sci.*, 1987, **28**, 65.
2 S. Vaucher, M. Li and S. Mann, *Angew. Chem., Int. Ed.*, 2000, **39**, 1793; J. Zhai, Y. Zhai, L. Wang and S. Dong, *Inorg. Chem.*, 2008, **47**, 7071; F. Shiba, R. Fujishiro, T. Kojima and Y. Okawa, *J. Phys. Chem. C*, 2012, **116**, 3394; W. Zhu, K. Liu, X. Sun, X. Wang, Y. Li, L. Cheng and Z. Liu, *ACS Appl. Mater. Interfaces*, 2015, **7**, 11575.
3 C. Li, Z. Hou, C. Zhang, P. Yang, G. Li, Z. Xu, Y. Fan and J. Lin, *Chem. Mater.*, 2009, **21**, 4598; P. Li, Y. Liu, Y. Guo, X. Shi, G. Zhu and H. Zuo, *Ceram. Int.*, 2015, **41**, 6620; J. Zou, Q. Zhu, X. Li, X. Sun and J.-G. Li, *J. Alloys Compd.*, 2021, **870**, 159380.
4 F. Shiba, T. Fujiwara, Y. Takeda and Y. Okawa, *CrystEngComm*, 2022, **24**, 2958.
5 I. Sunagawa, in *Crystals: Growth, Morphology and Perfection*, Cambridge University Press, Cambridge, 2005, ch. 4.
6 T. Sugimoto, in *Monodispersed Particles*, Elsevier, Amsterdam, 2nd edn, 2019, ch. 3.
7 I. H. Leubner, R. Jagannathan and J. S. Berry, *Photogr. Sci. Eng.*, 1980, **24**, 268; T. Sugimoto, *J. Colloid Interface Sci.*, 1983, **91**, 51.
8 S. Hamada, Y. Kudo and I. Ishiyama, *Shikizai Kyokaishi*, 1996, **69**, 658.
9 K. Chen, C. Sun, S. Song and D. Xue, *CrystEngComm*, 2014, **16**, 5257.
10 F. Shiba, M. Yuasa and Y. Okawa, *CrystEngComm*, 2018, **20**, 4910.
11 J. E. Maskasky, *J. Imaging Sci.*, 1986, **30**, 247.
12 M. Otomo and Y. Wakamatsu, *Bunseki Kagaku*, 1968, **17**, 764.
13 S. G. Duyker, G. J. Halder, P. D. Southon, D. J. Price, A. J. Edwards, V. K. Peterson and C. J. Kepert, *Chem. Sci.*, 2014, **5**, 3409.
14 F. Shiba, U. Mameuda, S. Tatejima and Y. Okawa, *RSC Adv.*, 2019, **9**, 34589; F. Shiba, A. Yamamoto, Y. Shinta, U. Mameuda, Y. Tahara and Y. Okawa, *RSC Adv.*, 2021, **11**, 8767.

15 F. Goubard and A. Tabuteau, *J. Solid State Chem.*, 2002, **167**, 34; H. Aono, T. Nishida, M. Kurihara, M. Sakamoto and Y. Sadaoka, *Ceram. Int.*, 2012, **38**, 2333.
16 W. A. Bentley and W. J. Humphreys, in *Snow Crystals*, Dover Publications, New York, 1962, pp. 50–73.
17 T. Kobayashi, *Philos. Mag.*, 1961, **6**, 1363.
18 W. F. Berg, *Proc. R. Soc. London, Ser. A*, 1938, **164**, 79.
19 E. Yokoyama and T. Kuroda, *Phys. Rev. A: At., Mol., Opt. Phys.*, 1990, **41**, 2038.
20 G. W. Beall, D. F. Mullica and W. O. Milligan, *Acta Crystallogr., Sect. B: Struct. Crystallogr. Cryst. Chem.*, 1978, **34**, 1446.
21 H. J. Buser, D. Schwarzenbach, W. Petter and A. Ludi, *Inorg. Chem.*, 1977, **16**, 2704; F. Herren, P. Fischer, A. Ludi and W. Hälg, *Inorg. Chem.*, 1980, **19**, 956.
22 A. Azhar, Y. Li, Z. Cai, M. B. Zakaria, M. K. Masud, Md. S. A. Hossain, J. Kim, W. Zhang, J. Na, Y. Yamauchi and M. Hu, *Bull. Chem. Soc. Jpn.*, 2019, **92**, 875.
23 S. Nakayama, M. Sakamoto, K. Matsuki, Y. Okimura, R. Ohsumi, Y. Nakayama and Y. Sadaoka, *Chem. Lett.*, 1992, 2145; E. Traversae, M. Sakamoto and Y. Sadaoka, *J. Am. Ceram. Soc.*, 1996, **79**, 1401.
24 M. Pidburtnyi, B. Zanca, C. Coppex, S. Jimenez-Villegas and V. Thangadurai, *Chem. Mater.*, 2021, **33**, 4249.
25 H. J. Kim, S. H. Kim, S.-W. Kim, J.-K. Kim, C. Cao, Y. Kim, U. Kim, G. Lee, J.-Y. Choi, H.-S. Oh, H.-C. Song, W. J. Choi, H. Park and J. M. Baik, *Nano Energy*, 2023, **105**, 108003.
26 H. Aono, M. Sato, E. Traversa, M. Sakamoto and Y. Sadaoka, *J. Am. Ceram. Soc.*, 2001, **84**, 341.
27 X. Liu, H. Xie and J. Mao, *J. Electroanal. Chem.*, 2022, **911**, 116228.
28 A. Zentko, M. Bokor, M. Lukáčová, M. Maryško, M. Mihalik, Z. Mitróová and M. Zentková, *Phys. Status Solidi A*, 2003, **196**, 340.
29 V. S. Perera, L. D. Yang, J. Hao, G. Chen, B. O. Erokwu, C. A. Flask, P. Y. Zavalij, J. P. Basilion and S. D. Huang, *Langmuir*, 2014, **30**, 11847; M. Perrier, A. Gallud, A. Ayadi, S. Kennouche, C. Porredon, M. Gary-Bobo, J. Larionova, Ch. Goze-Bac, M. Zanca, M. Garcia, I. Basile, J. Long, J. de Lapuente, M. Borrasd and Y. Guari, *Nanoscale*, 2015, **7**, 11899.